

High resolution imaging of young M-type stars of the solar neighbourhood: Probing the existence of companions down to the mass of Jupiter. [★]

P. Delorme¹, A.M. Lagrange¹, G. Chauvin^{1,2}, M. Bonavita³, S. Lacour⁴, M. Bonnefoy², D. Ehrenreich¹, and H. Beust¹

¹ UJF-Grenoble 1 / CNRS-INSU, Institut de Planétologie et d'Astrophysique de Grenoble (IPAG) UMR 5274, Grenoble, F-38041, France.

² Max Planck Institute for Astronomy, Königstuhl 17, D-69117 Heidelberg, Germany.

³ Department of Astronomy and Astrophysics, University of Toronto, 50 St. George Street, Toronto, Ontario, Canada M5S 3H4

⁴ LESIA, CNRS/UMR-8109, Observatoire de Paris, UPMC, Université Paris Diderot, 5 place Jules Janssen, 92195 Meudon, France.

ABSTRACT

Context. High contrast imaging is a powerful technique to search for gas giant planets and brown dwarfs orbiting at separation larger than several AU. Around solar-type stars, giant planets are expected to form by core accretion or by gravitational instability, but since core accretion is increasingly difficult as the primary star becomes lighter, gravitational instability would be the a probable formation scenario for yet-to-be-found distant giant planets around a low-mass star. A systematic survey for such planets around M dwarfs would therefore provide a direct test of the efficiency of gravitational instability.

Aims. We search for gas giant planets orbiting around late-type stars and brown dwarfs of the solar neighbourhood.

Methods. We obtained deep high resolution images of 16 targets with the adaptive optic system of VLT-NACO in the L' band, using direct imaging and angular differential imaging. This is currently the largest and deepest survey for Jupiter-mass planets around M-dwarfs. We developed and used an integrated reduction and analysis pipeline to reduce the images and derive our 2D detection limits for each target. The typical contrast achieved is about 9 magnitudes at 0.5'' and 11 magnitudes beyond 1''. For each target we also determine the probability of detecting a planet of a given mass at a given separation in our images.

Results. We derived accurate detection probabilities for planetary companions, taking into account orbital projection effects, with in average more than 50% probability to detect a $3 M_{\text{Jup}}$ companion at 10 AU and a $1.5 M_{\text{Jup}}$ companion at 20 AU, bringing strong constraints on the existence of Jupiter-mass planets around this sample of young M-dwarfs.

Conclusions.

1. Introduction

The discovery of extrasolar planets around solar analogs, initiated by Mayor & Queloz (1995), has radically modified our understanding of planetary formation. The new models that strive to describe planetary formation mechanisms need observational constraints on planetary companions on a large range of parameters, such as stellar mass, metallicity, planet mass and orbital parameters. Notably, the most prolific methods for exoplanet detection, radial velocities and transits, only cover separations up to a few AU and barely reaches the large separation range where all the Solar System giant planets reside. This range can be probed by direct high-resolution imaging. Only a few unambiguously planetary-mass companions to stars (Chauvin et al. 2004; Marois et al. 2008; Kalas et al. 2008; Lagrange et al. 2010) were discovered by direct imaging, but each one of these detections proved extremely valuable to constrain formation models. Until recently, core accretion (CA) was the preferred model to explain both our Solar System planets and the close-in giant planets found by radial velocity (RV) around solar-type stars. The recently imaged giant planets at large separations from their

parent A-type stars (Marois et al. 2008; Kalas et al. 2008) challenge however this simple view as they are very difficult to form *in situ* by CA, though Rafikov (2011) shows that under specific condition CA can form Jupiter-mass planets as far as 40-50AU. In the case of HR8799, this could account for the formation *in situ* of the 3 innermost planets, but Dodson-Robinson et al. (2009) claim that HR8799bcd formation by CA has to happen at closer separation and be followed by planet scattering at the observed separation, which would not create a stable system. Dodson-Robinson et al. (2009) claim that, instead, gravitational instability (GI) in a disc could produce the *bcd* planets *in situ* while Kratter et al. (2010) argue that HR8799bcd can be formed by GI, but only at larger separation and show that under certain conditions they can migrate to the separations where they are currently observed. However the innermost planet of this system, HR8799e (Marois et al. 2010) appears at least as difficult to form by GI as the outermost planet HR8799b would be to form by CA, hinting that planetary formation models still need improvement to be able to account for the first multi-exoplanetary system directly imaged and badly need further observational constraints, especially in different mass range, before drawing any strong conclusion on the respective part they actually play in planetary formation.

Planetary mass objects could also form in the same way as stars, with Bate (2009) showing that a few objects as light as $\sim 5 M_{\text{Jup}}$ can form by core fragmentation, possibly ending in

Send offprint requests to: P. Delorme, e-mail: Philippe.Delorme@obs.ujf-grenoble.fr

[★] Based on observations made with the NACO at VLT UT-4 at the Paranal Observatory under programs ID 084.C-0739, 085.C-0675(A), 087.C-0413(A) and 087.C-0450(B).

very high mass-ratio binary system, very look-alike to a planetary system. Such planetary-like binary system could also be formed by disc instabilities in a very massive primordial disc (Stamatellos et al. 2011), which could produce systems quite similar to 2M1207AB (Chauvin et al. 2004), together with numerous brown dwarfs and very low-mass stars.

The dependency of planetary formation modes to the stellar mass is an open field of investigation, with some observational clues that planetary masses, as well as disc masses, scale with stellar masses (e.g. Forveille et al. 2011; Scholz et al. 2006). Debris and transitional discs tracing planetary formation have been detected even around M dwarfs and brown dwarfs, with frequencies similar (Plavchan et al. 2009) or even larger (Currie & Sicilia-Aguilar 2011) than around solar-type stars.

Boley (2009) identifies some indications of bi-modal giant planets formation, but many more detections are needed to confirm this scenario. In that frame, looking for gas giant planets around M-type stars offers a distinct opportunity to test planet formation mechanisms, as models predict that CA is very inefficient (Kennedy & Kenyon 2008, KK08). KK08 predict a rate of 1% for CA formed giant planets around M stars if the rate is of 6% for G type stars) or “all but impossible” (DR09) in producing giant planets around those stars. The main reason being that there is not enough time to form cores with $5\text{-}10M_{\oplus}$ before the gas in the protoplanetary disk is dissipated. On the contrary, GI can be quite efficient in forming giant planets around M stars, at separations larger than typically 20 AU with Boss (2011) claiming that “even late M dwarf stars might be able to form gas giants on wide orbits”. This hints at the possibility that there are more giant planets at large separations around late-type stars than there are close-in ones.

From an observational point of view, most of the planets found so far around a yet small number of M-type stars are rather low-mass ($\leq 0.1 M_{\text{Jup}}$) ones, and in close orbits. The monitoring of M-type stars started recently and these active stars are complicated targets for RV searches; hence, the domain ≥ 3 AU is largely unexplored via RV technics. However the trend that massive giant planets are less common around M stars than around more massive stars at short separations seems statistically robust (e.g. Forveille et al. 2011, ; Bonfils et al. 2011, submitted). The picture at the larger separations (≥ 10 AU) is less clear cut. First, RV survey show that planetary frequency around M dwarfs increases as separation increases (Bonfils et al. 2011, submitted). Secondly this trend is supported by evidence from micro-lensing surveys, with Gould et al. (2010) showing that the frequency of Jupiter (respectively Saturn) mass planets at ~ 10 AU is about 10% (respectively 20%), and correlates well with the extrapolation of RV surveys to large separations.

This separation range started being explored with direct Adaptive Optic (AO) imaging in the recent years, on a small number of late type objects (17 out of 118 in the recent compilation of Nielsen & Close 2010), and with limited sensitivities (typically $>4 M_{\text{Jup}}$). Others surveys targeted at young late M stars and brown dwarfs were very sensitive to unequal mass binary systems ($q \sim 0.2$; Ahmic et al. 2007; Biller et al. 2011) but did not reach mass ratio typical of planetary systems ($q < 0.01$), and therefore did not probe the supposedly more numerous light giant planets ($\leq 1 M_{\text{Jup}}$) that are supposed to be more frequent at large separation around M dwarfs.

The main limitation of high resolution imaging of M-dwarfs is their intrinsic faintness which makes difficult to achieve good AO correction from the ground. Spatial observations (e.g. Bouy et al. 2003) and Laser Guide Star observations (e.g. Biller et al. 2011) do mitigate this issue but make high-resolution deep

observations of M dwarf more challenging than similar observations around solar-type stars. However, since most of M dwarfs flux is emitted in the infrared, the capabilities of VLT-NAOS adaptive optics system with Infrared Wave-Front Sensor (IRWFS) significantly broaden the sample of M dwarfs which can be used as a good quality natural guide star, thus enabling their observations at high Strehl ratio from the ground. Given the very red Spectral Energy Distribution (SED) of Jupiter mass planets, typically $K_s - L' = 3.3$ at $3 M_{\text{Jup}}$ and $K_s - L' > 6$ at $1 M_{\text{Jup}}$ at 30 Myr (according to BT-SETTL 2010 models, Allard & Freytag 2010), observing in the L' band offers a greatly enhanced sensitivity to the lowest mass planets. The additional capability of NACO to observe in the L' range therefore makes NACO at VLT a unique instrument to probe for planets around M dwarfs. The high spatial density of M-type stars in the solar neighbourhood makes it easier to build a good sample of young and nearby low-mass stars than it is for solar-type stars. Their youth ensures a more favourable contrast for planetary companions and their intrinsically low flux enable to probe much lower companion masses around M dwarfs than around any other stars for a given contrast. We therefore started a direct imaging survey in L' with NACO to look for giant planets around young nearby M-dwarfs in stellar associations, and probe separations down to a few AU and masses down to $\sim 0.5 M_{\text{Jup}}$. We describe our sample and observations in section 2, and detail our data analysis methods in section 3. Our results are presented in section 4.

2. The stars

2.1. Sample selection

We built a sample large enough to be statistically significant of young late-type stars close and young enough to ensure optimal detection and separation limits. We selected all late-type stars younger than 50 Myr (for early M stars) and 100 Myr (for $\geq M4V$ stars), closer than 45 pc, among the members of nearby young associations, identified notably by Torres et al. (2008); Lépine & Simon (2009); Kiss et al. (2011). For the latest type targets, we furthermore kept only those brighter than $K_s = 12$, to have a good AO correction. We removed targets members of known low contrast, seeing-resolved, close binary systems with separations between $0.5''$ and $1.5''$ that could confuse the wave front analysis and lower the quality of the AO correction. We ended up with a sample of 52 targets (46 M0-M5 and 6 M8+). We present here observations of 16 stars from this sample, detailed on table 1, which were observed during our first observing nights for this program.

2.2. Observations

Since low-mass stars are fainter in the visible and brighter in the infrared, we used NACO with its Infrared Wave Front Sensor (IWFS) to achieve good adaptive optic correction on these late-type targets. To lessen the contrast between stars and companions, we observed at $3.8\mu\text{m}$, in the L' band, where planets are brighter than in the near infrared. Depending on the brightness and hour angle of each targets at the time of the observations, we conducted either classical imaging (9 targets) and pupil tracking observations (7 targets).

We observed 11 targets in L' with NACO at VLT during the run 084.C-0739, from December 25th to December 29th, 2009 under average conditions, with seeing varying from 0.6 to $1.2''$, with a few excursions down to $0.5''$ and up to $1.5''$. During run 085.C-0675(A), on July 28th, 2010, 2 additional objects were

observed under moderate seeing conditions ($\geq 1''$), and variable absorption. Three new objects were observed during run 087.C-0413(A) under excellent conditions, with seeing varying in the 0.4-0.8'' range. Finally we obtained new L' -band observation of one of our target with NACO at VLT during run 087.C-0450(B) on September 1st, 2011, with seeing conditions of $\sim 0.8''$.

All objects presented here were observed in L' band with NACO, using the L27 camera, giving a 0.027'' per pixel sampling, and the ‘‘Uncorrelated and high well depth’’ detector mode. As detailed in table 1, we recorded data cubes of 100 to 400 very short exposures (0.075s to 0.4s), at the same position, totalling typically 30-60s time on target per cube. Several cubes were obtained, with a typical total exposure time of ~ 30 minutes, achieved following a 4-position dither pattern to ensure correct background subtraction. The AO loop was closed on these relatively faint and red targets using the infrared-wave front sensor with the ‘‘JHK’’ dichroic.

2.3. Estimation of the age of the stars in the sample

To convert the observed companions fluxes into masses or to estimate the detection probability in term of masses, one needs to use brightness-mass relations, which are strongly dependent on the age of the system.

2.3.1. Targets belonging to young moving groups

In this case the age determination is relatively straightforward since we can assume that a star has the age of its parent moving group. Following Torres et al. (2008) and references therein we assumed an age of 8 Myr for members of TW Hydrae, 12 Myr for β pic members, 30 Myr for Tucana-Horologium members and 70 Myr for AB Doradus members.

2.3.2. 2MASSJ044337.6+000205.2

This object is not known as young moving group member but is identified as a low gravity M9 by Cruz et al. (2007) and as having lithium absorption (Reiners & Basri 2009). This implies the object is a brown dwarf below lithium burning mass or a slightly higher mass star/brown dwarfs that has not yet burned all its lithium. Using BT-SETTL models, it appears that this combination of spectral type and lithium absorption is only possible for an object younger than ~ 120 Myr. We therefore present detection probabilities both for a young age hypothesis of 50 Myr and an old age hypothesis of 120Myr.

2.3.3. HIP114046/GI887

This object is not either known as young moving group member which makes its age determination more challenging. Indeed, even if this very nearby M2 star (3.3pc) is identified in Simbad as a pre-main sequence star, different age estimation methods give wildly different values. Pasinetti Fracassini et al. (2001) CADARS catalog that compiles angular diameters gives very high radius estimates (respectively 0.62 and 0.56 R_{\odot}), derived by Lacy (1977); Johnson & Wright (1983) from parallax and visual apparent magnitude. According to BT-SETTL models this would mean HIP114046 is aged of about 30-50 Myr. However the corresponding near-infrared colours would not fit the 2MASS colours, and the near-infrared magnitudes would be more than 1 magnitude too bright. Using V, J, H, K magnitudes

Table 2. Rotation periods and corresponding Gyrochronological ages derived for HIP114046 assuming different value for the inclination angle i . Errors are derived using a 10% error on the $v \cdot \sin i$ measurement and the dispersion around the age/period relation observed in the Hyades by Delorme et al. (2011).

i (deg.)	Rotation Period(days)	Age(Myrr)
0	17.7	1060 \pm 200
30	15.3	820 \pm 150
45	12.6	<625
60	8.9	<625

and the corresponding colours together with its spectral type of M2 (~ 3700 K) and comparing with BT-SETTL models, we derive that HIP114046 is probably a 0.5-0.55 M_{\odot} star aged anywhere between 100 Myr and 10 Gyr, with a radius of approximately 0.35 R_{\odot} . The strong discrepancy in radius with earlier work is difficult to explain but could be linked to the strong improvement of M dwarfs models in the last 30 years. According to Ehrenreich et al. (2011), this object is not very active in X ray ($R_x = -5.13$), giving more weight to the hypothesis that the object is not very young. The high absolute proper motion of this star, also points toward an older age. On the opposite, the detection of lithium absorption (Torres et al. 2006) favours a very young age (below ~ 30 Myr), that is difficult to reconcile with its apparent luminosity.

We try in the following to bring more quantitative constraints on the age of HIP114046 using gyrochronology (see Barnes 2003, for instance). There are $v \sin(i)$ measurements of rotational velocities on the star of 1.0 $km \cdot s^{-1}$ by Nordström et al. (2004), where v is the rotational velocity at the equator and i is the inclination of the axis of rotation with respect to the line of sight. Assuming the diameter of 0.35 R_{\odot} given by BT-SETTL models for HIP114046, and assuming various values for i , we used the relations between rotational periods and age given by Delorme et al. (2011) to derive the ages listed in table 2. This indicates that HIP114046 is probably younger than 1Gyr and is also compatible with a much younger age. We cannot derive a lower limit on the age of HIP114046 because the $i > 45^{\circ}$ hypothesis brings the rotation period in the range of relatively fast M dwarfs rotators that have not converged yet toward the clean age-period relation on which gyrochronology is grounded. Within this hypothesis, HIP114046 would be younger than the convergence time for early M dwarfs, but could not have its age more accurately measured by gyrochronology. Since the convergence time for early M-dwarfs has been measured by Delorme et al. (2011); Agüeros et al. (2011) to be about the age of the Hyades (~ 625 Myr Perryman et al. 1998), $i > 45^{\circ}$ would mean HIP114046 could have any age between 0 and ~ 625 Myr. In this article we present detection probabilities of HIP114046 both for a young age hypothesis of 100 Myr and a conservatively old age hypothesis of 2000Myr.

3. Data analysis

3.1. Image reduction

All images were reduced using the IDL pipeline developed for AO reduction at the Institut de Planétologie et d’Astrophysique de Grenoble (IPAG), that we describe in the following.

Table 1. Targets information. Pupil tracking indicates observations were carried out in pupil tracking and with a field rotation enabling ADI reduction procedures.

Target Name	Coordinates		Spectral Type	Membership	Date Obs.	Exposure Time (Seconds)	Comments
	RA	Dec					
GSC08056	02 36 51.5	-52 03 04.4	M2	Tuc-Hor	26/12/2009	91×150×0.2	Pupil Tracking
GJ3305	04 37 37.5	-02 29 28.2	M0	β pic	26/12/2009	64×300×0.2	Binary; Pupil Tracking
GJ3305	04 37 37.5	-02 29 28.2	M0	β pic	01/09/2011	250×150×0.2	Binary; Pupil Tracking
2MASS J0443	04 43 37.6	+00 02 05.2	M9	(1)	27/12/2009	50×300×0.2	Pupil Tracking
V1005 Ori	04 59 34.8	+01 47 00.7	M0	β pic	25/12/2009	16×150×0.2	-
CD-571054	05 00 47.1	-57 15 25.5	M0V	β pic	29/12/2009	64×150×0.2	-
BD-21 1074A	05 06 49.6	-21 35 06.0	M2V	β pic	28/12/2009	32×120×0.25	-
BD01 2447	10 28 55.6	+00 50 27.6	M2.5V	AB Dor	02/05/2011	48×200×0.2	Pupil Tracking
2M1139	11 39 51.1	-31 59 21.5	M8	TWA	26/12/2009	36×600×0.3	-
2MASS1207	12 07 33.5	-39 32 53.9	M8	TWA	26/12/2009	141×300×0.2	-
TWA25	12 15 30.7	-39 48 42.6	M1V	TWA	03/05/2011	24×100×0.4	-
TYC7443-1102-1	19 56 04.4	-32 07 37.7	M0V	β pic	03/05/2011	87×200×0.2	Pupil Tracking
HIP102409/AUmic	20 45 09.5	-31 20 27.2	M1V	β pic	28/07/2010	94×100×0.2	Pupil Tracking
WWPsA	22 44 58.0	-33 15 01.7	M1	β pic	27/12/2009	32×150×0.2	-
TXPsA	22 45 00.0	-33 15 25.8	M5V	β pic	26/12/2009	32×150×0.2	-
HIP114046	23 05 52.0	-35 51 11.1	M2V	(2)	28/07/2010	92×100×0.2	Pupil Tracking
BD-13 64 24	23 32 30.9	-12 15 51.4	M0V	β pic	27/12/2009	32×150×0.2	-

References. (1) Presence of lithium according to Reiners & Basri (2009) and low gravity (Cruz et al. 2007) ensures this object is younger than 120Myrs (see section 2.3.2). (2) Age determination is presented in section 2.3.3. For mass limit determination purposes we assumed an age range of 100-2000 Myr.

3.1.1. Bad pixels removal, flat-fielding and recentering

To achieve optimal flat-fielding and bad pixel removal we acquire sky flats for each detector/dichroic/filter combination used for each run. The raw data are flat-fielded and bad pixels are removed using these twilight flat images. The background for each data cube is calculated from the median of all cubes observed within 250s of the reduced cube and subtracted to each frame within a cube. The quality of these individual reduced frames is assessed to remove frames for which the AO loop was open or the AO correction was poorer than usual. This automatic selection process makes use of the cubes statistics of flux peak and total flux in the image to remove these lower quality frames. The remaining good-quality intra-cube frames are then accurately re-centered using Moffat fitting, before each cube is collapsed to produce one image. Each of these collapsed image is then re-centered again using Moffat fitting to ensure they all are centred at the same position.

3.1.2. Additional reduction steps for Angular Differential Imaging

Seven of our targets were observed with the rotator off and at an hour angle that allowed sufficient field rotation (typically $\geq 25^\circ$) to use simple ADI reduction method (Marois et al. 2006) to remove the PSF of the central star.

We used several advanced variations on the ADI technic on each of these targets, namely smart ADI (Lagrange et al. 2010), LOCI (Lafrenière et al. 2007), and the new slightly different method that we describe here, “weighted” ADI. Weighted-ADI is a variant of “smart” ADI. The references used to build the smart-ADI PSF for a given image are chosen with the constraint that the field must have rotated by a given angle with respect to the image, to mitigate the self-subtraction of possible companions. The n references closest in time to the image, with n being a free parameter that we usually set to 10, are then median-combined to produce the PSF that will be subtracted to the image. Since the PSF evolve with time, a natural step beyond smart

ADI is to weight each reference by a value related to the invert of the time-span between image and reference before combining them. We used a weighted-ADI method working exactly as a smart ADI but for the use of $\frac{1}{\Delta t}$ as a weight for each reference. As can be seen in table 3 the method yields results that are slightly better compared to smart-ADI, and particularly interesting in case of moderate on-sky rotation ($\leq 30^\circ$).

3.1.3. Additional reduction steps for classical imaging

Ten of our targets were observed in classical imaging mode, with field tracking on. For these we also used independently several subtraction methods, namely low frequency spatial filtering (a sliding median filter with a box size of $4 \times \text{FWHM}$), subtraction of radial profile (for a given annulus centred on the primary, we subtract the median value of all pixels within the annulus) and subtraction of the image rotated by π .

For all targets, whether or not observed in ADI, a stacked image of the full NACO field of view, extended by the offset of the dither pattern was produced to search for background-limited large separation companions. Since most of our observations were windowed to 512×512 pixels, the resulting field was $19.5 \times 19.5''$, typically 400 AU by 400 AU on sky. In the case of 2M1207, the full 1024×1024 frame was read, resulting in a four-fold increase in the research area.

3.2. Companion detection tools

3.2.1. Automatic check for candidates

Given the different possible signatures of a companion in residual images of AO observations once reduced with the various ADI technics, the trained human eye is usually the most efficient way of looking for companions in the speckle-dominated region close to the star. See Fig. 4 for an example of a target with a confirmed and a possible companion after ADI subtraction. However, searching by eye lacks objectivity and does not

allow to obtain quantitative value of the threshold above which potential companions are investigated. Additionally, in the background dominated region far from the central star, automatic routines can be more reliable than eyeballing to systematically look for low Signal to Noise (hereafter SN) companions in this relatively large area.

In order to have an objective way of looking for companions in our final residual image we built an automatic detection routine that works as follows:

- We create a detection map which is the residual image median-boxed on 3 pixels.
- The successive maxima of this detection map are investigated as a potential companions. This detection image is not used afterwards but enables to distinguish between detections caused by remaining bad pixels or similar artefact from more reliable detections.
- For each maximum the local background and noise are estimated as the median and the dispersion of pixels values within the intersection of 2 annuli in the initial residual image, one centred around the central star and another around the candidate itself.
- The resulting SN of the candidate on $1.5 \times \text{FWHM}$ -diameter aperture is derived, and is tested against a user-defined SN threshold.
- If this test is passed, a Moffat fit on the core of the signal is carried out. This fit is severely constrained so that it does not differ wildly from the expected FWHM-wide Moffatian of the core of a true PSF and mitigate the effects of ADI self-subtraction, as described below.
- A new SN, using the flux of the Moffatian fit under a $1.5 \times \text{FWHM}$ -diameter aperture centred on the peak of the flux, is derived.
- If this SN is higher than a given threshold, the candidate is pinpointed as a potential companion that needs to be confirmed by a visual inspection complemented by regular outputs from the fit, such as the χ^2 .

The rationale we used to mitigate the effects of ADI self-subtraction is the following. Firstly, the fit is carried out on a small aperture, typically within the first Airy ring. This excludes most of the negative ADI-signatures of the companion (see Fig. 1) which would mathematically lower the signal of a companion while they actually enhance our confidence in a detection. Secondly, the fit is weighted to artificially give more weight to the central pixels which are less affected by self-subtraction.

3.2.2. Visual check for candidates

Though the fit produces useful information regarding the shape of the detected sources, it is not reliable enough, especially in the speckle-dominated area, to use as a tool for final candidate selection. Our strategy was therefore to assist human inspection of residual images with the detection routine, which provided a map of the 3σ automatic detections and their corresponding fit parameters. The subsequent human inspection of these sources allowed to retain only the most credible candidates, usually corresponding to a signal to noise higher than $\sim 5\sigma$.

3.2.3. 2D detection limits maps

We took a particular care to derive accurate and meaningful detection limit map around each of our targets.

The first step was to produce a noise map of each of our final residual image, by measuring the pixel noise within sliding

square boxes of 5×5 pixels (typically $\sim 1.5 \times \text{FWHM}$). This provides the noise per pixel and could be used directly to derive the peak value of a signal that would be above a given SN threshold. However, since actual detections do not rely on a single pixel being above a signal to noise threshold, we preferred to derive the 5σ detection limit on a $1.5 \times \text{FWHM}$ -diameter aperture, comparing the noise within the aperture to the flux of the unsaturated PSF of each target within the same aperture.

In the case of ADI-reductions, a second step was to correct these detection maps from the flux loss caused by self-subtraction. We created cubes of images of high SN fake planets with the same field rotation as the science images and applied the same ADI procedures as used for the science images. We compared the flux injected to the flux recovered by our detection pipeline on the final reduced fake planets images (see Fig. 1) to derive the actual flux loss due to self-subtraction in ADI-processing on a range of radius from the central star. Note that since these fake planet images are used to measure only self-subtraction effects, the central star is not included in the image. The effects of the central star residuals are already taken into account in the noise map produced in the previous step, where it dominates the local noise at short separations.

Finally, the detection limit in Arbitrary Detector Unit was converted into a contrast in magnitudes by scaling it to the measured flux of the unsaturated science target. Figure 2 shows one instance of such a contrast map where the target is a close binary to illustrate the advantages of a 2D mapping approach over a 1D detection limit curve in a strongly asymmetrical case.

Such 2D contrast maps were produced for all targets and for all the reduction technics used. Tables 3 and 4 give the median of the contrast achieved in each image both for a close separation area (< 18.5 pixels = $0.5''$) and a wider separation area (> 18.5 pixels and < 100 pixels = $2.7''$). Inner pixels for which there was not enough rotation to find a suitable PSF reference either in LOCI or sADI/wADI were removed from the statistics of all reduction modes. Computing values over area rather than annuli, and using the same pixels for each set of images, provides robust statistics to quantitatively compare different reduction technics. Note that these tables present detection limits obtained with a single set of ADI and LOCI parameters and that slightly better detection limits (typically by ≤ 0.3 mag) can be obtained by manually fine tuning the parameters for each target, especially when using LOCI. We carried out such optimised analysis each time we had a hint that a potential candidate companion could be visible, but since the overall sensitivity gain was modest, we choose to present the more self-consistent detection limits obtained with a single set of parameters for all targets.

4. Results

4.1. Specially interesting targets

We detail case by case a few specifically interesting objects, notably 2 targets around which we identified candidate companions, none of which were physically associated with the central star.

4.1.1. 2M1139/TWA26

Our automatic detection routine identified a source 13σ above local background, at a separation $\rho = 13.4''$ and a position angle $\theta = 196^\circ$ from 2M1139, at RA = 11:39:50.8 and Dec = -31:59:34.8

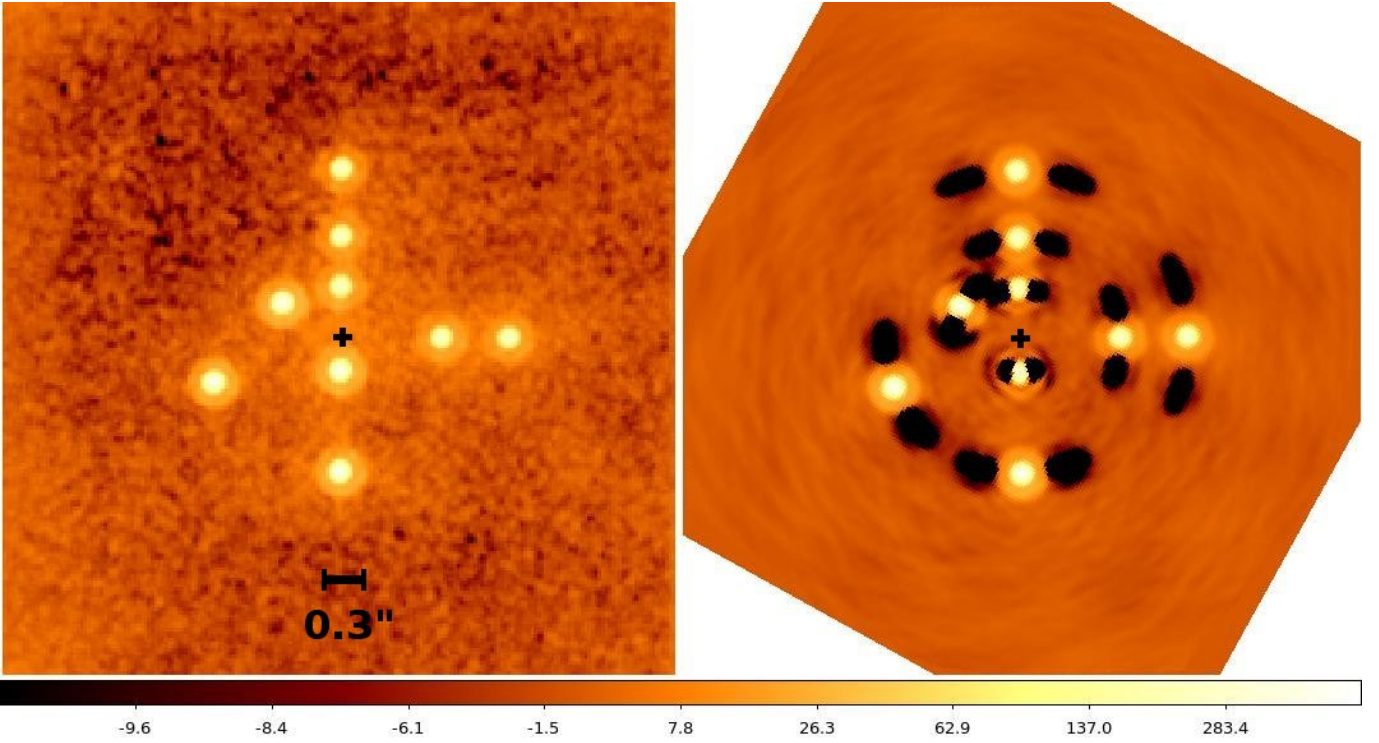


Fig. 1. **Left:** False colour image of fake planets injected at separation ranging from $0.27''$ to $1.35''$ in a cube with the same sky rotation as the science target. **Right:** Residual image of these fake planets after weighted-ADI procedure were applied, simulating an on-sky rotation of 29° . Self-subtraction effects are visible as negatives “wings” around the fake planets. The rotation centre for the ADI procedure is marked by a black cross. A logarithmic scale is used.

Table 3. Median contrast achieved for ADI-compatible observations, ranked by field-rotation, at 5σ limit for short ($\leq 0.5''$) and large separation areas. Best values are highlighted in bold.

Target Name	Simple ADI		Smart ADI		Weighted ADI		LOCI		Sky Rotation (Degree)
	$\leq 0.5''$	$> 0.5''$	$\leq 0.5''$	$> 0.5''$	$\leq 0.5''$	$> 0.5''$	$\leq 0.5''$	$> 0.5''$	
BD01 2447	9.1 ± 0.15	12.69 ± 0.02	9.3 ± 0.11	12.46 ± 0.03	9.9 ± 0.14	12.53 ± 0.03	9.7 ± 0.11	12.09 ± 0.02	23
GSC0856	8.8 ± 0.07	9.90 ± 0.02	8.7 ± 0.08	9.70 ± 0.02	8.9 ± 0.08	9.79 ± 0.02	8.3 ± 0.08	9.38 ± 0.02	29
2MASS J0443	5.8 ± 0.06	6.84 ± 0.02	6.1 ± 0.06	6.71 ± 0.02	6.2 ± 0.06	6.74 ± 0.02	6.1 ± 0.06	6.54 ± 0.02	29
GJ3305 (12/2009)	9.1 ± 0.26	11.37 ± 0.02	8.9 ± 0.27	11.24 ± 0.03	9.0 ± 0.28	11.30 ± 0.03	9.2 ± 0.20	11.07 ± 0.03	40
HIP114046	9.6 ± 0.15	14.23 ± 0.03	9.9 ± 0.15	14.04 ± 0.03	9.8 ± 0.17	14.05 ± 0.03	10.1 ± 0.10	13.34 ± 0.04	47
GJ3305 (09/2011)	9.6 ± 0.27	11.47 ± 0.03	9.1 ± 0.20	11.15 ± 0.03	9.3 ± 0.20	11.23 ± 0.03	9.7 ± 0.21	11.21 ± 0.04	50
HIP102409/AUmic	9.4 ± 0.15	13.16 ± 0.03	8.8 ± 0.14	12.90 ± 0.03	9.1 ± 0.17	12.95 ± 0.03	10.2 ± 0.10	12.73 ± 0.04	74
TYC7443-1102-1	9.3 ± 0.09	9.84 ± 0.02	8.9 ± 0.09	9.72 ± 0.02	9.0 ± 0.08	9.78 ± 0.02	8.6 ± 0.07	9.33 ± 0.02	95

A check of 2MASS images shows a $H=15.5$ object at the position of our L' detection. Since this object was also detected in USNO optical images, where it appears much brighter than the central star it is obviously too blue and too bright to be a lower mass companion of 2M1139. This was further confirmed by its proper motion which is not compatible with the proper motion of 2M1139, at more than 10σ .

4.1.2. The GJ3305 AB system

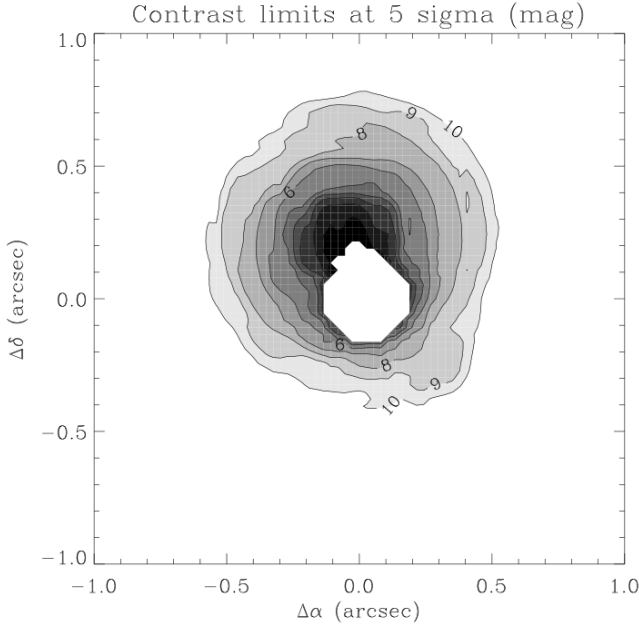
GJ3305B. GJ3305 has been identified by Kasper et al. (2007) as a low contrast close binary. Figure 4 shows the reduced image side to side with the residual map after simple ADI subtraction. GJ3305B appears clearly in both images at a PA of 19.2° and a separation of $0.27''$. Its Airy rings are visible in the residual image up to the 6th, a telltale sign of the effectiveness of the primary subtraction. By combining archive data of GJ3305AB shown on table 5 with our L' observations we have 7 indepen-

dent astrometric measurements of GJ3305B. Since they are relatively regularly spread on a significant fraction of the full orbit we attempted a Levenberg-Marquardt fit of an orbit for the system. We fixed the mass of this 12Myr-old β Pictoris moving group system to $0.85 \pm 0.5 = 1.35 M_\odot$ using stellar evolution models from Baraffe et al. (2003). Though we don't have enough astrometric points to derive accurate orbital parameters, the fit consistently converged towards solutions where the orbit is seen nearly edge-on ($i \sim 93^\circ$), with a low eccentricity ($e \sim 0.05$), with a resulting period of 20-25 years, and a semi-major axis of 8-9 AU, see Fig. 3. Since only about one third of the orbital period is covered by observations, the uncertainties are high and it is not currently possible to accurately constrain the mass of the system.

Candidate companion to GJ3305AB. Another interesting source was identified around GJ3305AB in Dec. 26, 2009 im-

Table 4. Median contrast achieved at 5σ limit over a short($\leq 0.5''$) separation area and a large separation area for targets observed with classical AO imaging (without ADI mode).

Target Name	Circular Profile Subtraction		Subtraction of π -Rotated Image	
	$\leq 0.5''$	$> 0.5''$	$\leq 0.5''$	$> 0.5''$
V1005 Ori	7.5 ± 0.18	10.28 ± 0.03	7.0 ± 0.15	9.89 ± 0.02
CD-571054	7.5 ± 0.12	11.52 ± 0.03	7.1 ± 0.10	11.25 ± 0.03
BD-21 1074A	7.6 ± 0.14	11.11 ± 0.03	7.2 ± 0.14	10.83 ± 0.03
2M1139	5.5 ± 0.10	5.80 ± 0.02	5.1 ± 0.09	5.47 ± 0.02
2MASS1207	6.5 ± 0.09	6.65 ± 0.02	6.1 ± 0.14	6.34 ± 0.02
WWPsA	7.6 ± 0.14	10.12 ± 0.02	7.1 ± 0.12	9.74 ± 0.02
TX PsA	7.3 ± 0.12	9.13 ± 0.02	6.7 ± 0.11	8.75 ± 0.02
TWA25	7.1 ± 0.14	9.75 ± 0.03	6.7 ± 0.13	9.37 ± 0.02
BD-136424	7.7 ± 0.15	10.45 ± 0.03	7.2 ± 0.14	10.09 ± 0.03


Fig. 2. Final contrast map for the GJ3305AB system. Contours identify magnitudes of contrast at 5σ achieved at a given position. The white area in the centre shows the position of the primary where no contrast was measurable and dark zone slightly on the north is the higher noise area induced by GJ3305B. North is up and East is left.

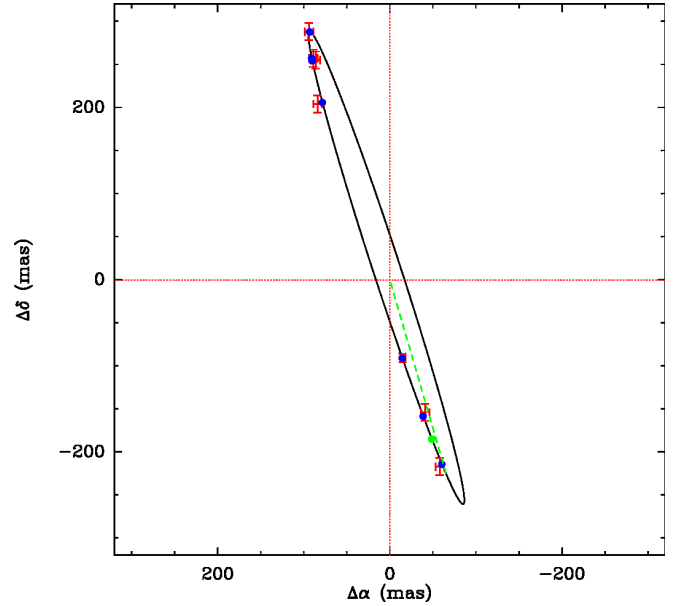
ages, at a PA of $224\pm 2^\circ$ and a radius of $0.38''$ from GJ3305A. Since this source sits opposite to GJ3305B and between its Airy rings it is located in a relatively clean area of the residual map and the automatic detection routine identifies it as a 6 to 11 σ detection in all the different residuals maps produced with the different ADI technics. It was however located very close to the second Airy ring of the primary, and could be a speckle. Though it is likely this 2009 source was affected by speckle noise on the Airy ring, it was significantly above this local noise and the presence of ADI negative signatures around it supported it as real on-the-sky source rather than a speckle artefact.

The resulting contrast with the primary in L' is ~ 9 magnitudes, far too faint to be detected at similar separations in all but one of the earlier dataset of GJ3305, the December 15th 2004, NACO L' data from which GJ3305B was initially identified. We retrieved the data from ESO archive and reduced it. Unfortunately given the lower exposure time and the now super-

Table 5. Position angle and separation of GJ3305B over the years. Typical separation error is 1mas and angle error is 1 deg.

Date	Radius (mas)	Position Angle ($^\circ$)	Instrument-Filter
18/01/2003	225	195	NACO-IB _{2.09} ¹
08/01/2004	159	194	NACO-NB _{2.12}
15/12/2004	93	189.5	NACO- L' ¹
17/11/2008	221	20.5	NTT/Astralux- z' ²
25/11/2009	269	18.6	NACO- L'
26/12/2009	272	19.2	NACO- L'
01/09/2011	303	18.1	NACO- L'

References. ¹ From Kasper et al. (2007). ² From Bergfors et al. (2010)


Fig. 3. Best fit for GJ3305B orbit projected on the sky in black, corresponding to a period of 21.5yr, and eccentricity of 0.06, a semi-major axis of 8.5 AU and an inclination of 93.2° . Observational astrometric points are in blue and the periastron is highlighted in green.

sed ADI technics used for these observations, the noise at the position -assuming it is physically associated- of the faint candidate companion was higher than its expected signal and could not be used to confirm the detection. In the hypothesis this object would be a background source, the proper motion of GJ3305 is too low and not radial enough (RA= $+46 \text{ mas.yr}^{-1}$ and Dec=-

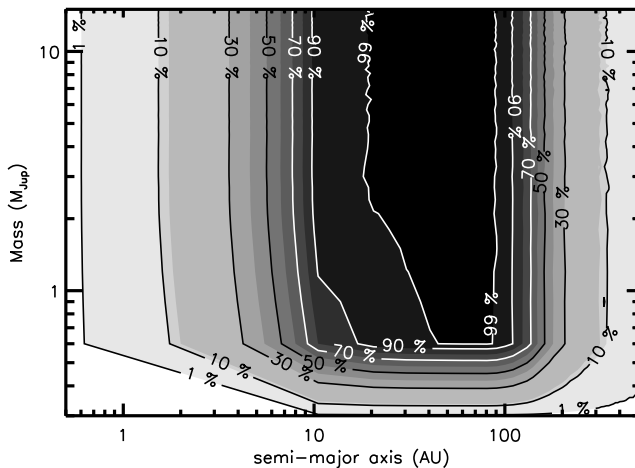


Fig. 5. Planetary detection probability around AU Mic. Numbers on the contours indicate the detection probability, taking into account the projection effects that could hid a planet in the line of sight of the central star on a fraction of its orbit. The semi-major axis values are therefore in real AU and not in projected AU.

65 mas.yr⁻¹) to bring the source out of the speckle dominated area, where it would have been detectable. Since we could not either rule out this hypothesis on the basis of archive data, further observations were necessary.

These observations were carried out with NACO at VLT on September 1st, 2011 and reduced following the ADI procedures described in section 3. The exposure time, rotation and the resulting detection limits for these new observations were slightly higher than those achieved on the 2009 data on which the candidate companion was identified. No source is detected in 2011 in the -small- area compatible with the orbital motion of a 11 AU planetary companion to GJ3305AB. This source is therefore not a planetary companion. A faint source is located close to the position expected if the 2009 detection was a background object. However the flux measured on this source in 2011 is ~ 0.7 magnitude fainter than the flux of the 2009 candidate, raising doubt on the physical nature of both detections. As a consequence, these data cannot establish whether the 2009 candidate was a background object or a speckle noise bump, but they allow to exclude it as a planetary companion. The residual images at both dates are shown on Fig. 4.

4.1.3. AU Mic/HIP102409

AU Mic. is known to harbour a edge-on debris disc (Song et al. 2002) which has been imaged using HST/ACS coronagraphy down to 7.5 AU (Krist et al. 2005). Their HST images shows no significant trace of gravitational perturbation of the disc by a large planetary body at close separation. We derived accurate detection probabilities as described in section 4.2 and show that our data are able to exclude the presence of a planetary companion as light as $0.6 M_{\text{Jup}}$ beyond 20 AU with $>90\%$ confidence (see Fig. 5), and improves the previous non-detections by Krist et al. (2005) and Kasper et al. (2007). Note that since our detection limits show some sensitivity down to Saturn mass objects, below the lowest masses available in the AMES-DUSTY model grid ($0.5 M_{\text{Jup}}$), we extrapolated values between $0.3 M_{\text{Jup}}$ and $0.5 M_{\text{Jup}}$, resulting in higher uncertainties in this mass range.

4.2. Constraints on the existence of planetary mass companions

In order to evaluate the giant-planet detection probability around the targets in our survey, we used the MESS code (Bonavita et al. 2011). For each star, the code generates 103 orbits per grid point in a mass versus semi-major axis (SMA) grid with a sampling of 0.5 AU in SMA axis and 0.5 M_{Jup} in mass. The orbits are randomly oriented in space, and the eccentricities were also randomly generated with a uniform distribution (with $e < 0.6$). For each random event, the code then evaluates the projected separation and the position of the planet on the projected orbit at the time of the observation. With this approach we can take into account possible projection effects, and then constraint the actual semi-major axis of the planets, instead of the projected separation, while also using the whole spatial information coming from the 2D detection limit maps evaluated in Sec. 3.2.3. The mass limits are obtained by translating these flux detection limits into mass using the COND-base models (Allard et al. 2001; Baraffe et al. 2003) for temperatures below 1700 K and DUSTY-based models (Chabrier et al. 2000) for higher temperatures. The mass of the artificial planet is then compared to the detectable mass at that position on the detection map, and the fraction of orbits at each grid point that turn out to be detectable then corresponds to the probability of detection at that grid point.

The resulting detection probability for each target are showed in Fig. 6. Figure 7 illustrates the mass detection limits of the full survey, by averaging the 14 mass detection probabilities maps of our targets with an accurate age measurement, and therefore excluding HIP114046 and 2M0443. The decreasing detection probability for very large semi-major axis reflects the fact that such objects can be observed within our $19.5 \times 19.5''$ field of view only on a fraction of their orbit and for favorable combination of eccentricity and angle of sight. Using the full 52 star sample, these limits could be used to derive constraints on the existence of giant planets around late-type stars and consequently on planetary formation models around low-mass stars. However, the sub-sample of 16 stars we present here is too small to be derive meaningful statistics and more observations are needed to bring it to a statistically more robust size.

5. Conclusion

We presented the results of the deepest imaging survey of young M dwarfs to date, using L' imaging with NACO at VLT. After developing a dedicated reduction and analysis pipeline, we achieved detection limits in average down to $1.5 M_{\text{Jup}}$ beyond 20 AU and up to 100-200 AU, and $3 M_{\text{Jup}}$ at 10 AU. On the closest and latest type targets we achieved detection limits well below the mass of Jupiter beyond 10 AU, therefore actually starting to probe (on 5 objects) the mass/separation range where planets around M dwarfs are supposed to be more frequent (Gould et al. 2010, Bonfils et al, submitted), but found none. We also probed the high planetary mass range ($M < 13 M_{\text{Jup}}$) at close separations, reaching planetary sensitivity at 5 AU or less on 9 out of our 16 targets. In spite of these deep observations we found only one planetary companion, 2M1207B, discovered by Chauvin et al. (2004), in this sample of young M dwarfs. Unfortunately, our sample is currently too small to derive meaningful constraints on the existence of giant planets around late type stars, beyond the simple statement that giant planets more massive than $1 M_{\text{Jup}}$ are not common. With the same statistical limitations, our data also support the “brown dwarfs desert” hypothesis (Halbwachs et al. 2000) down to the lowest brown

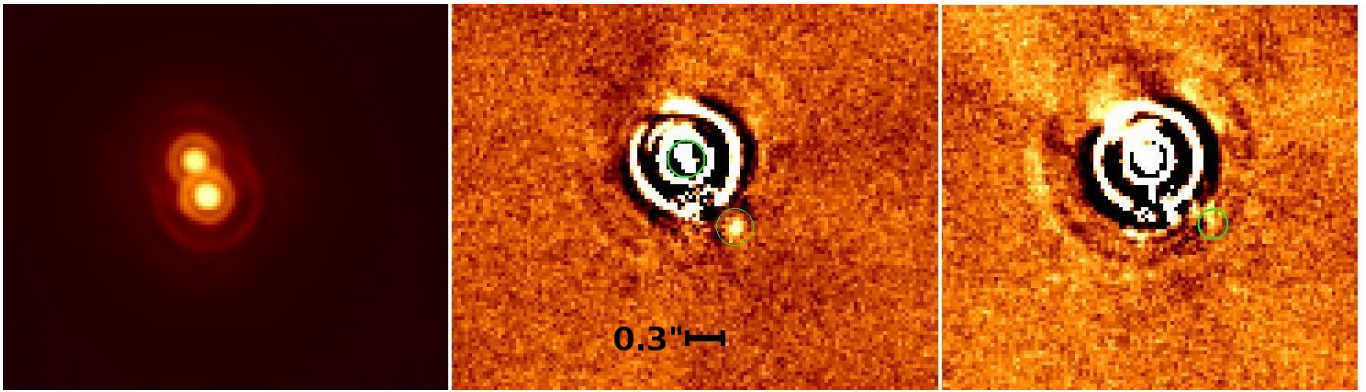


Fig. 4. **Left:** Final stacked false-colour image of GJ3305AB from December 2009 data, in L' . North is up and East is left. Logarithmic scale is used. **Center:** Residual image of GJ3305AB from December 2009 data, after GJ3305A is subtracted by simple ADI. GJ3305B and the candidate companion are highlighted with green circles. Linear scale is used. **Right:** Residual image of GJ3305AB from September 2011 data, after GJ3305A is subtracted by simple ADI. No source is detected at the 2009 position of the 2009 source. The position expected for this source in case it was a background object is highlighted by a green circle. Linear scale is used. North is up and East is left.

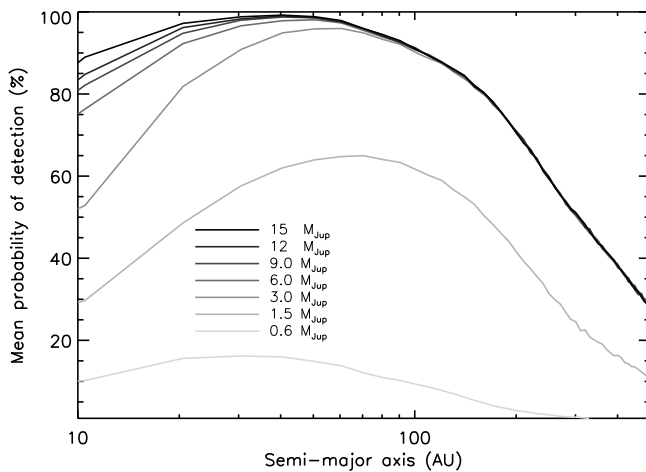


Fig. 7. Summary of the detection probabilities of the survey for a range of companion masses, obtained by averaging the detection probabilities of the 14 targets with an accurate age determination. The semi-major axis values are therefore in real AU and not in projected AU.

dwarfs masses, since we found no brown dwarfs companions while our survey had in average more than 95% de-projected sensitivity to brown dwarfs beyond 15 AU and could discover a fraction of them as close as 5 AU from the central star. Further deep observations in L' of such targets are necessary to increase our statistical significance and to bring stronger constraints on formation models around low-mass stars.

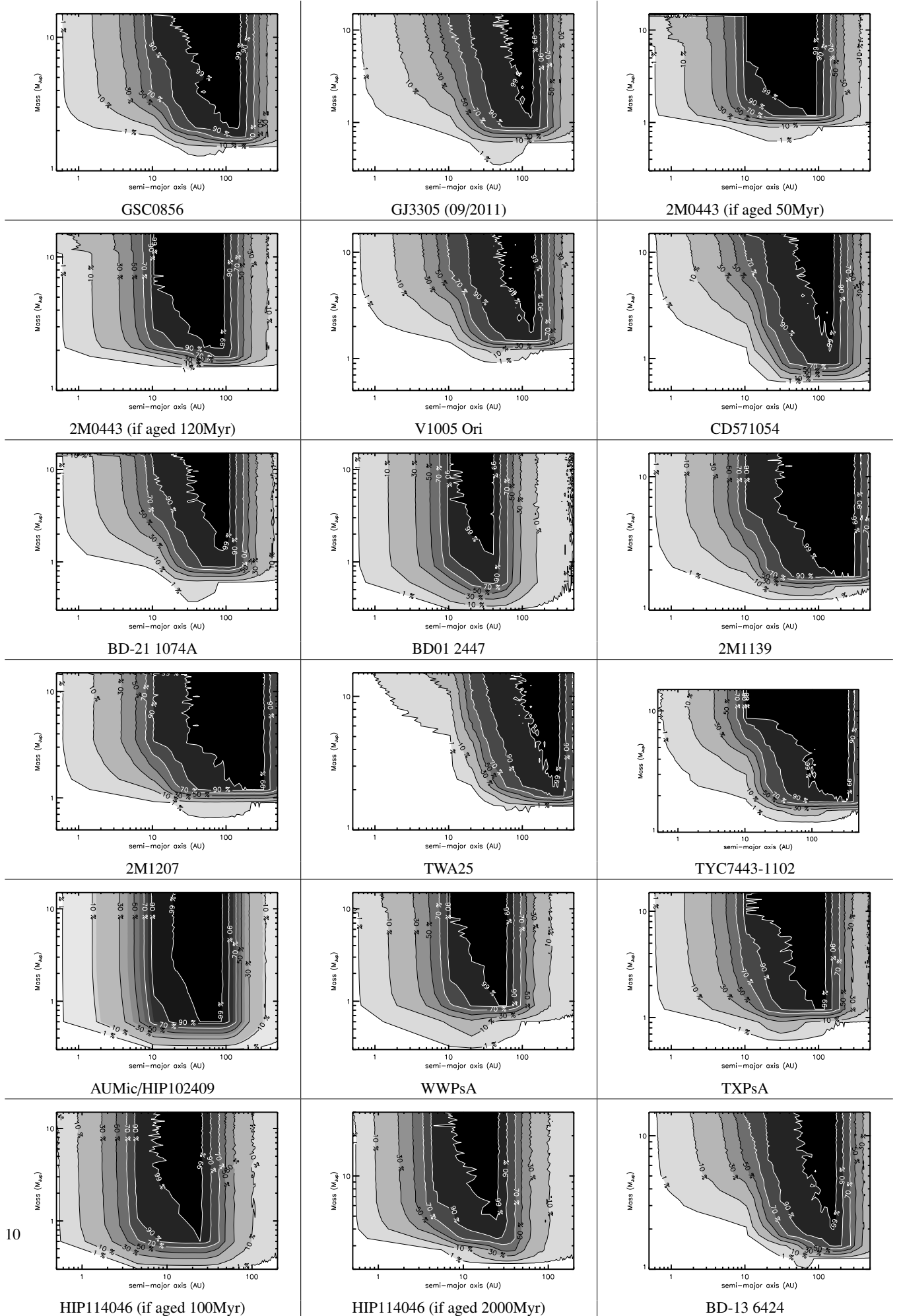
Acknowledgements. We acknowledge financial support from the French Programme National de Planétologie (PNP, INSU) and from the French National Research Agency (ANR) through the GuEPARD project grant ANR10-BLANC0504-01. P.D. was financed by a grant from the Del Duca foundation. We thank David Lafrenière for his precious help with the LOCI code. This research has made use of the VizieR catalogue access tool, of SIMBAD database and of Aladin, operated at CDS, Strasbourg. We thank the referee for his accurate comments.

References

Agüeros, M. A., Covey, K. R., Lomonias, J. J., et al. 2011, *ApJ*, 740, 110

- Ahmic, M., Jayawardhana, R., Brandeker, A., et al. 2007, *ApJ*, 671, 2074
 Allard, F. & Freytag, B. 2010, *Highlights of Astronomy*, 15, 756
 Allard, F., Hauschildt, P. H., Alexander, D. R., Tamanai, A., & Schweitzer, A. 2001, *ApJ*, 556, 357
 Baraffe, I., Chabrier, G., Barman, T. S., Allard, F., & Hauschildt, P. H. 2003, *A&A*, 402, 701
 Barnes, S. A. 2003, *ApJ*, 586, 464
 Bate, M. R. 2009, *MNRAS*, 392, 590
 Bergfors, C., Brandner, W., Janson, M., et al. 2010, *A&A*, 520, A54+
 Biller, B., Allers, K., Liu, M., Close, L. M., & Dupuy, T. 2011, *ApJ*, 730, 39
 Boley, A. C. 2009, *ApJ*, 695, L53
 Bonavita, M., Chauvin, G., Desidera, S., et al. 2011, *ArXiv e-prints*
 Boss, A. P. 2011, *ApJ*, 731, 74
 Bouy, H., Brandner, W., Martín, E. L., et al. 2003, *AJ*, 126, 1526
 Chabrier, G., Baraffe, I., Allard, F., & Hauschildt, P. 2000, *ApJ*, 542, 464
 Chauvin, G., Lagrange, A.-M., Dumas, C., et al. 2004, *A&A*, 425, L29
 Cruz, K. L., Reid, I. N., Kirkpatrick, J. D., et al. 2007, *AJ*, 133, 439
 Currie, T. & Sicilia-Aguilar, A. 2011, *ApJ*, 732, 24
 Delorme, P., Collier Cameron, A., Hebb, L., et al. 2011, *MNRAS*, 413, 2218
 Dodson-Robinson, S. E., Veras, D., Ford, E. B., & Beichman, C. A. 2009, *ApJ*, 707, 79
 Ehrenreich, D., Lecavelier Des Etangs, A., & Delfosse, X. 2011, *A&A*, 529, A80
 Forveille, T., Bonfils, X., Lo Curto, G., et al. 2011, *A&A*, 526, A141+
 Gould, A., Dong, S., Gaudi, B. S., et al. 2010, *ApJ*, 720, 1073
 Halbwachs, J. L., Arenou, F., Mayor, M., Udry, S., & Queloz, D. 2000, *A&A*, 355, 581
 Johnson, H. M. & Wright, C. D. 1983, *ApJS*, 53, 643
 Kalas, P., Graham, J. R., Chiang, E., et al. 2008, *Science*, 322, 1345
 Kasper, M., Apai, D., Janson, M., & Brandner, W. 2007, *A&A*, 472, 321
 Kennedy, G. M. & Kenyon, S. J. 2008, *ApJ*, 673, 502
 Kiss, L. L., Moór, A., Szalai, T., et al. 2011, *MNRAS*, 411, 117
 Kratter, K. M., Murray-Clay, R. A., & Youdin, A. N. 2010, *ApJ*, 710, 1375
 Krist, J. E., Ardila, D. R., Gólimowski, D. A., et al. 2005, *AJ*, 129, 1008
 Lacy, C. H. 1977, *ApJS*, 34, 479
 Lafrenière, D., Marois, C., Doyon, R., Nadeau, D., & Artigau, É. 2007, *ApJ*, 660, 770
 Lagrange, A.-M., Bonnefoy, M., Chauvin, G., et al. 2010, *Science*, 329, 57
 Lépine, S. & Simon, M. 2009, *AJ*, 137, 3632
 Marois, C., Lafrenière, D., Doyon, R., Macintosh, B., & Nadeau, D. 2006, *ApJ*, 641, 556
 Marois, C., Macintosh, B., Barman, T., et al. 2008, *Science*, 322, 1348
 Marois, C., Zuckerman, B., Konopacky, Q. M., Macintosh, B., & Barman, T. 2010, *Nature*, 468, 1080
 Mayor, M. & Queloz, D. 1995, *Nature*, 378, 355
 Nielsen, E. L. & Close, L. M. 2010, *ApJ*, 717, 878
 Nordström, B., Mayor, M., Andersen, J., et al. 2004, *A&A*, 418, 989
 Pasinetti Fraccasini, L. E., Pastori, L., Covino, S., & Pozzi, A. 2001, *A&A*, 367, 521
 Perryman, M. A. C., Brown, A. G. A., Lebreton, Y., et al. 1998, *A&A*, 331, 81
 Plavchan, P., Werner, M. W., Chen, C. H., et al. 2009, *ApJ*, 698, 1068
 Rafikov, R. R. 2011, *ApJ*, 727, 86

Fig. 6. Detection probability as a function of the mass and semi-major axis of the planets obtained with the MESS code (see text), for all the targets.



- Reiners, A. & Basri, G. 2009, *ApJ*, 705, 1416
Scholz, A., Jayawardhana, R., & Wood, K. 2006, *ApJ*, 645, 1498
Song, I., Weinberger, A. J., Becklin, E. E., Zuckerman, B., & Chen, C. 2002, *AJ*, 124, 514
Stamatellos, D., Maury, A., Whitworth, A., & André, P. 2011, *MNRAS*, 413, 1787
Torres, C. A. O., Quast, G. R., da Silva, L., et al. 2006, *A&A*, 460, 695
Torres, C. A. O., Quast, G. R., Melo, C. H. F., & Sterzik, M. F. 2008, *Young Nearby Loose Associations*, ed. Reipurth, B., 757–+